High-Detectivity All-Polymer Photodiode Empowers Smart Vitality Surveillance and Computational Imaging Rivaling Silicon Diodes

Hrisheekesh Thachoth Chandran, Ruijie Ma,* Zhihan Xu, Jipsa Chelora Veetil, Yongmin Luo, Top Archie Dela Peña, Iyappan Gunasekaran, Sudhi Mahadevan, Kuan Liu, Yin Xiao, Hao Xia, Jiaying Wu, Mingjie Li, Sai-Wing Tsang, Xinge Yu, Wen Chen,* and Gang Li*

Near-infrared (NIR) organic photodetectors (OPDs), particularly all-polymer-based ones, hold substantial commercial promise in the healthcare and imaging sectors. However, the process of optimizing their active layer composition to achieve highly competitive figures of merit lacks a clear direction and methodology. In this work, celebrity polymer acceptor PY-IT into a more NIR absorbing host system PBDB-T:PZF-V, to significantly enhance the photodetection competence, is introduced. The refined all-polymer ternary broadband photodetector demonstrates superior performance metrics, including experimentally measured noise current as low as 6 fA Hz$^{-1/2}$, specific detectivity reaching 8×10^{12} Jones, linear dynamic range (LDR) of 145 dB, and swift response speed surpassing 200 kHz, striking a fair balance between sensitivity and response speed. Comprehensive morphological and photophysical characterizations elucidate the mechanisms behind the observed performance enhancements in this study, which include reduced trap density, enhanced charge transport, diminished charge recombination, and balanced electron/hole mobilities. Moreover, the practical deployment potential of the proof-of-concept device in self-powered mode is demonstrated through their application in a machine learning-based cuffless blood pressure (BP) estimation system and in high-resolution computational imaging across complex environments, where they are found to quantitatively rival commercial silicon diodes.

1. Introduction

The demand for near-infrared (NIR) light detectors is rapidly increasing due to their advanced scientific and industrial applications in health monitoring, surveillance systems, artificial vision, imaging, optical coherence tomography, etc.[1] Present-day NIR photodetectors are primarily constructed using materials such as silicon or compound inorganic semiconductors, including indium gallium arsenide (InGaAs) and mercury cadmium telluride (HgCdTe). These materials are indeed expensive to produce due to complex manufacturing processes that often require high-purity materials, sophisticated fabrication facilities, and advanced technology. Additionally, InGaAs and HgCdTe detectors often involve costly epitaxial growth processes and need to be cooled for optimal performance, which adds to the overall expense. Moreover, the resolution of commercial NIR imaging sensors is typically limited by the need for precise alignment between the silicon read-out integrated circuitry

H. T. Chandran, R. Ma, K. Liu, H. Xia, G. Li
Department of Electrical and Electronic Engineering
Research Institute for Smart Energy (RISE)
Photonics Research Institute (PRI)
The Hong Kong Polytechnic University
Hung Hom, Kowloon, Hong Kong SAR, P. R. China
E-mail: ruijie.ma@polyu.edu.hk; gang.w.li@polyu.edu.hk

Z. Xu, Y. Xiao, W. Chen
Department of Electrical and Electronic Engineering
The Hong Kong Polytechnic University
Hung Hom, Kowloon, Hong Kong SAR, P. R. China
E-mail: owen.chen@polyu.edu.hk

J. C. Veetil, I. Gunasekaran, X. Yu
Hong Kong Center for Cerebro-Cardiovascular Health Engineering (COCHE)
Hong Kong, SAR, P. R. China

Y. Luo, T. A. Dela Peña, J. Wu
Function Hub
Advanced Materials Thrust
The Hong Kong University of Science and Technology
Nansha, Guangzhou 511400, P. R. China

(ROIC) and the photoactive layer, which constrains the pixel pitch to ≈10 μm.[2,3] The fabricated inorganic PDs are inherently rigid and fragile, and do not meet the new-generation applications in the healthcare industry, which demands flexible, stretchable, and skin conformable photodiodes. Provided with the material specific limitations described above, the scientific community is in search of cheaper alternative materials with competitive detection and mechanical characteristics.

Organic semiconductors can ideally be considered as a potential alternative due to their excellent opto-electronic and mechanical characteristics.[4,5] The detection range of organic materials can be tuned to NIR or short-wave infrared (SWIR) region via chemical modifications and the organic sensing layer can be directly processed over ROIC.[6–9] It is noted that the NIR detectors are essential in health diagnostics, particularly in point-of-care devices that favor NIR light sources for their non-invasive properties.[10] In addition, OPDs can be fabricated over flexible and stretchable substrates at low temperature using cost-effective solution processing methods, providing an overall advantage over inorganic PDs for emerging applications.

Organic photovoltaic (OPV) devices that employ non-fullerene acceptors (NFAs) have expanded the selection of materials for the photosensitive active layers of OPDs.[11,12] These functional materials have led to OPV devices achieving a power conversion efficiency (PCE) of up to 19% in binary configurations and even higher efficiencies, reaching up to 19.9%, in ternary systems.[13–17]

Most of the high-performance OPDs reported so far use a polymer donor and non-fullerene small molecule acceptor (NFSMA) like ITIC, Y6 and their derivatives.[11,18] Despite their success in realizing highly sensitive PDs, the below par operational stability and difficulty in reproducibility are adversely affecting the practical viability of NFSMA based PDs. In addition, to meet the demands of flexible and stretchable wearable devices with extended operational lifetimes, PDs based on NFSMAs may not be promising due to NFSMA's tendency for high diffusion, sharp domain interfaces, and morphological instabilities within the photosensitive layers.[19] However, the all-polymer PDs consisting of both π-conjugated polymer donor and polymer acceptor can address many of these concerns and have a great potential for practical applications.[19] Devices based on polymer acceptors typically offer several advantages over those using NFSMAs, including enhanced thermal and environmental stability, improved compatibility with polymer donors, higher absorption coefficients, easily adjustable energy levels, greater mechanical flexibility, and superior adaptability to roll-to-roll printing techniques like blade coating, as well as more effective control over blending and

morphology.[19] However, there are only handful of studies reported on all-polymer photodiodes with photodetection properties extending to NIR.[20–22] The common challenges encountered by NIR PDs, including simultaneously achieving high responsivity, minimizing dark/noise currents, and ensuring rapid response times, also pose significant obstacles for all-polymer PDs. This is attributed to factors such as increased thermal emission, high density of trap states, intense charge recombination, and limitations on charge transport.[20,23] Moreover, in-depth reports on photophysical and morphological studies revealing the photodetection features and kinetics of all polymer PDs are currently lacking and remain to be further explored.

In this work, we first designed and synthesized a new narrow bandgap polymerized small molecule acceptor (E_g^{opt} = 1.31 eV) and realized a binary all polymer NIR photodiode with broadband sensing competence extending up to 930 nm. Then, a second polymer acceptor with a relatively larger bandgap is incorporated into the binary host system to significantly improve the overall NIR PD performance. The optimized all polymer ternary system exhibits a dark current of 7 nA cm^{-2}, responsivity of 0.44 A W^{-1}, experimentally derived noise current as low as 6 fA Hz$^{-1/2}$, specific detectivity approaching 10^{13} Jones, a broad linear dynamic range (LDR) of 145 dB and an ultra-fast temporal response of 220 kHz at a reverse bias of −0.1 V. Although ternary systems have better detection properties than their binary parental counterparts, the photophysical process behind this enhancement is rarely investigated, specifically in all-polymer ternary PD systems. The photo physical behavior of the binary system and its transition to the optimized ternary system are investigated using ultra-fast spectroscopy and morphological evolution studies. We found that the detection capabilities of ternary devices are significantly improved when the morphology, exciton and trap behaviors are precisely controlled. The optimized ternary system has decreased trap density, balanced electron/hole mobilities, and improved recombination/transport kinetics. The proof-of-concept device with such high detectivity and response speed is used to demonstrate two feasible prototypes for real world applications. First, a point of care vitality surveillance system is developed by forming a photoplethysmography (PPG) sensor, and the collected data is trained using a machine learning model for feasible deployment. In addition, an advanced single-pixel imaging (SPI) system is demonstrated with Fourier transform algorithm on different imaging conditions; from free space to complex imaging environment where in the light must pass through the scattering grits and the detector is facing the wall instead of the target. More importantly, the performance of the all-polymer photodiode is quantitatively comparable with the default silicon detector. This study emphasized the important role of all polymer systems in realizing high performance organic photodiodes, investigated viable strategies to improve performance metrics over binary counterparts, and demonstrated advanced functionalities in real-world scenarios.

2. Results and Discussion

The synthesis route of the newly designed PZF-V polymer acceptor is given in Figure S1 (Supporting Information), and the synthesis procedure of the intermediate and final products are explained in detail in supporting information. The

T. A. Dela Peña, M. Li
Faculty of Science
Department of Applied Physics
The Hong Kong Polytechnic University
Kowloon, Hong Kong, P. R. China

S. Mahadevan, S.-W. Tsang
Department of Materials Science and Engineering
Center of Super-Diamond and Advanced Films (COSDAF)
Hong Kong Institute of Clean Energy (HKICE)
City University of Hong Kong
Hong Kong SAR, P. R. China
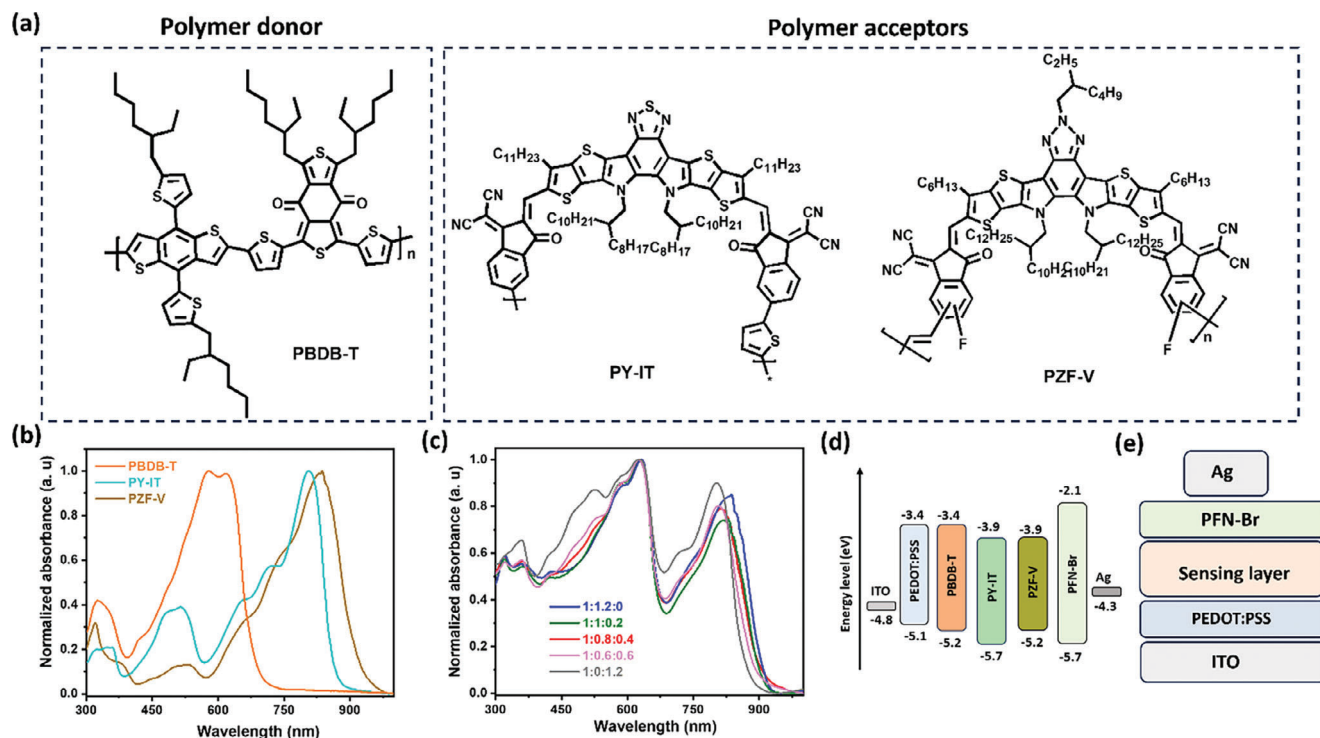
Figure 1. a) Chemical structure of the polymer donor and acceptor materials used in this study. Normalized absorption spectra of b) the pristine materials and) the blend films with different compositions. d) Flat band energy levels of the pristine materials and e) the schematic representation of the device architecture.

intermediate and final compounds are confirmed by the MALDI-TOF MS and NMR spectra (Figures S2–S5, Supporting Information). The absorption spectra of the PZF-V polymer in solution and thin film are given in Figure S6 (Supporting Information), and the optical bandgap is estimated as 1.31 eV. The cyclic voltammetry (CV) scans to estimate the highest occupied molecular orbital (HOMO), TGA plot and DSC plots are given in Figures S7–S9 (Supporting Information).

The device structure adopted in this study consists of ITO/PEDOT:PSS (30 nm)/ active layer (300 nm)/ PFN:Br (10 nm)/ Ag (80 nm). Here, ITO is the anode, Ag is the cathode, PE-DOT:PSS and PFN-Br are employed as charge blocking layers (CBL)/ charge transport layers (CTL). The sensing layer, irrespective of binary or ternary matrix, consists only of polymer materials and the chemical structures of the corresponding materials are given in **Figure 1a**. The binary device-1 (1:1.2:0) employs PBDB-T as the donor material and the newly designed PZF-V as the acceptor material. When the third component (PY-IT) is added to the binary matrix, ternary devices with compositions 1:1:0.2, 1:0.8:0.4, and 1:0.6:0.6 are formed. To have a more reasonable performance comparison, another binary structure (1:0:1.2) is fabricated with PBDB-T and PY-IT as D and A materials. The full names of the chemicals used are provided in Supporting Information. The absorption spectra of the pristine materials and the blended films used in this study are given in Figure 1b,c, the flat band energy level diagram is given in Figure 1d, and the schematic of the device architecture is given in Figure 1e. It is important to note that the energy levels obtained using the CV method are for individual pristine materials and do not ac-

count for interface energetics or the aggregation behavior observed in thin films. In actual film stacks within the PD architecture, there are sufficient driving forces for charge separation, as evidenced by the enhanced light responsivity discussed in a later section of the manuscript. The active layers of binary and ternary devices are maintained to be similar in thickness (300 ± 10 nm). It is noted that the polymer acceptors used in this study with similar molecular weight and low viscosity may not result in larger thickness variation among binary and ternary devices.

Next, the performance metrics of the binary and ternary all polymer PDs are investigated in detail. The dark/light current density-voltage (*J-V*) characteristics of studied devices are given in **Figure 2a** and Figure S10 (Supporting Information). The J_{light} values gradually increased from 1:1.2:0 binary device to 1:0:1.2 binary device and the ternary devices have values ranging between binary devices (Figure S10a, Supporting Information). Considering dark *J-V* characteristics, all of the devices have lower J_d values, and ternary devices have the lowest values among them. Considering 1:0.6:0.6 device, the J_d values are 0.5 nA cm^{-2} at self-power mode (0 V), 7 nA cm^{-2} at −0.1 V and 50 nA cm^{-2} at -1 V. These values are respectively 0.8 nA cm^{-2}, 13 nA cm^{-2} and 150 nA cm^{-2} for 1:1.2:0 device, representing higher values than ternary device but highly comparable or at best better than the all-polymer devices reported before.[20,21] In order to consider the active layer thickness into account, the J_d is plotted as a function of electric field, and exhibits an identical trend observed before (Figure S10b, Supporting Information). For a more detailed comparison among the ternary and binary devices, the statistical analysis is

**ADVANCED
SCIENCE NEWS**

www.advancedsciencenews.com

**ADVANCED
MATERIALS**

www.advmat.de
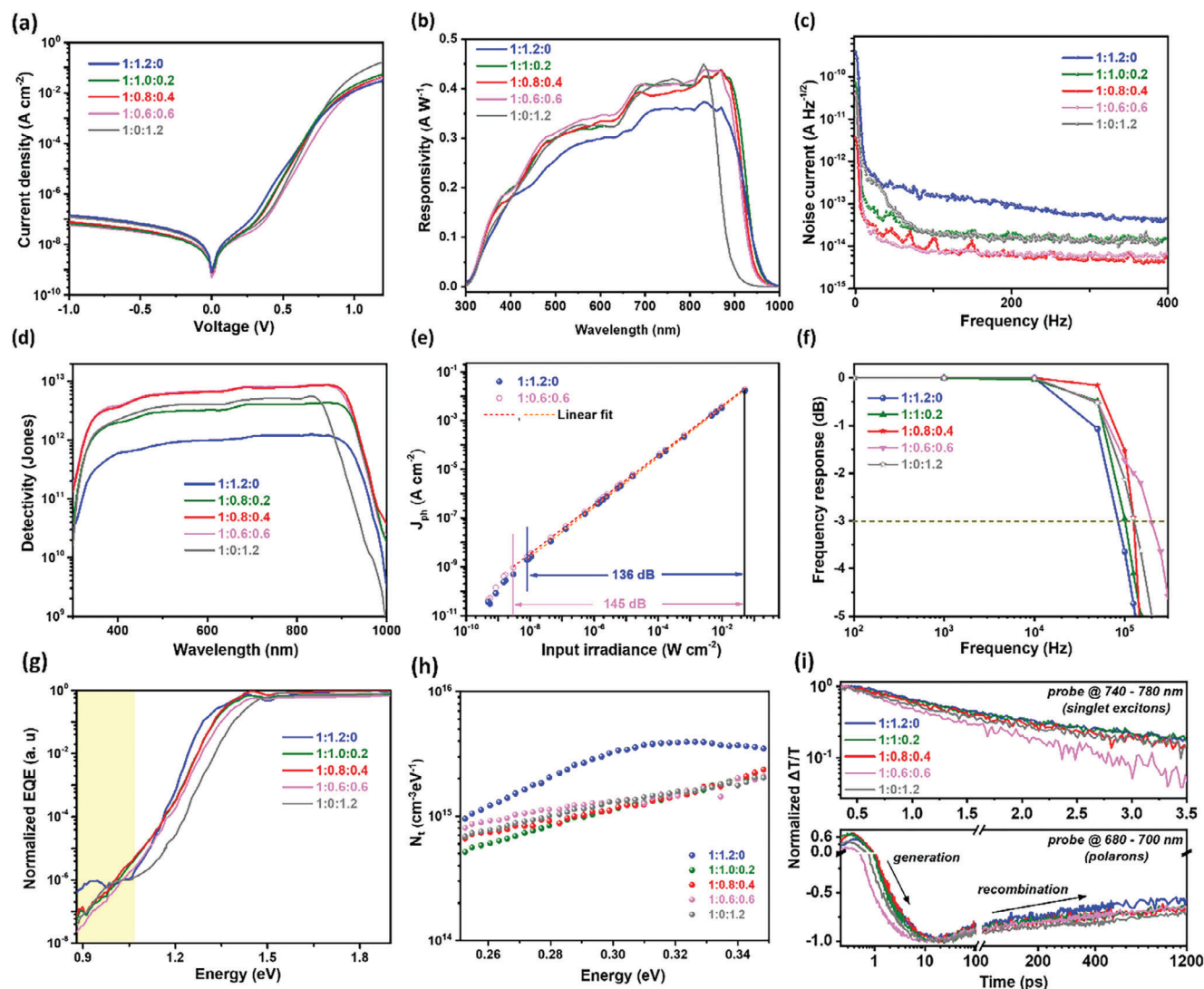
Figure 2. a) The dark *J-V* characteristics, b) responsivity, c) noise current, and d) the specific detectivity of the all-polymer PDs with different component ratios. e) LDR of the binary all-polymer PD and the representative ternary all polymer PD. f) -3 dB frequency of the all-polymer photodiodes explored in this study. g) Sensitive EQE spectra of all polymer PDs with different compositions and the shaded regime represents the trap state region. h) N_t distribution as a function of defect energy level for devices with different compositions and i) the corresponding dynamics of excitons and polarons from fs transient absorption spectroscopy (fs-TAS) with excitation wavelength set at 800 nm.

given in Figure S10c,d (Supporting Information). The mean J_d values at −0.1 and −1 V clearly show lower values for all three ternary compositions, in comparison to the binary devices. Unless otherwise specified, the remaining figures of merits are measured at −0.1 V bias.

Next, the responsivity (*R*), defined as the ratio of electrical output per optical input in units of A W^{-1} is derived by,

$$R = EQE \times q\lambda/hc \qquad (1)$$

where *EQE* stands for external quantum efficiency, *q* for charge, *λ* for wavelength, *h* for Planck constant and *c* for the speed of light. Let us consider the binary control device, the spectral coverage expands from 350 to ≈930 nm with a peak *R* value of

0.38 A W^{-1} ≈830 nm. Once the PY-IT is added to the binary matrix, there is a significant increase in the *R* value throughout the spectral range. For instance, 1:1.0:0.2 device has a peak value of 0.44 A W^{-1} which is ≈20% increase in peak value compared to the binary device. An increase in PY-IT content does not considerably enhance the peak R value, but the overall EQE value rises slightly, and the spectrum coverage gradually started shifting to the PY-IT absorption regime. Thus, we prefer not to raise the PY-IT loading by more than 50% in order to avoid further blue shift in spectral coverage. From the dark *J-V* characteristics and *R* spectra, the ternary devices are having a clear-cut advantage over the binary devices, but it is still hard to distinguish which ternary composition is performing better.

2407271 (4 of 13)

ADVANCED
SCIENCE NEWS

www.advancedsciencenews.com

**ADVANCED
MATERIALS**

www.advmat.de

Specific detectivity is among the most important performance metrics of photodiodes and is given by

$$D^* = \frac{R\sqrt{A}}{i_n} = \frac{\sqrt{A}}{NEP} \tag{2}$$

In Equation (2), it is clear that the R and noise current (i_n) are the deciding factors of D^*. The reported D^* values in the literature vary by orders of magnitude because of the method adopted for deriving the i_n. The most common method is to estimate the noise as the sum of shot noise and thermal noise, or at worst case simply omit the thermal noise and count shot noise as the sole source of noise.[24] These methods generally provide higher D^* values which is higher than the D^* derived from the experimentally determined noise current values. As a reliable method, we have experimentally obtained the noise current value using a network analyzer and is given in Figure 2c. The values at 210 Hz (the chopper frequency employed for responsivity measurement) are 86 fA Hz$^{-1/2}$ (1:1.2:0), 16 fA Hz$^{-1/2}$ (1:1.0:0.2), and ≈6 fA Hz$^{-1/2}$ for both 1:0.8:0.4 and 1:0.6:0.6 devices. There is a trend of suppressing the noise current when PY-IT is added as the third component to the binary systems. From the experimentally obtained noise current and R values, the D^* is obtained and is given in Figure 2d. The binary control device has a peak D^* of 1.1×10^{12} Jones and a value of $>1 \times 10^{11}$ Jones over the entire spectral range (350–950 nm), denoting excellent broadband detection characteristics. On the other hand, for ternary devices, the peak D^* value is increased to 4×10^{12} Jones (for 1:1:0.2) and to ≈8×10^{12} Jones for 1:0.8:0.4 device. Increasing the PY-IT content does not result in further increment in D^* value, suggesting the ideal composition is either 1:0.8:0.4 or 1:0.6:0.6. It is important to note that the D^* values for all polymer ternary devices reported in this work remains among the best reported values for state-of-the-art organic photodiodes, including both small molecule acceptor based PDs and all-polymer PDs.[11,18,23,25–28]

LDR is another important figure of merit of photodetector, defining the input light illumination range across which the detector output scales linearly with the input irradiance and is derived by

$$LDR = 20\log\frac{J_{upper}}{J_{lower}} = 20\log\frac{L_{upper}}{L_{lower}} \tag{3}$$

where L stands for input irradiance in W cm^{-2} and J stands for photocurrent density in A cm^{-2} and the upper and lower values stand for the maximum and minimum irradiance and photocurrent values. The LDR is derived from a double logarithmic plot, where the linear fit should have a slope of unity. It should be noted that the unity slope plays a critical role in defining the divergence point from linearity, and the deviation from unity slope can substantially overestimate the LDR value.[29] We examined the LDR of a binary device (1:1.2:0) and a representative ternary device (1:0.6:0.6) and is depicted in Figure 2e. The binary device has an LDR value of 136 dB with a deviation point of 8×10^{-9} W cm^{-2}, while the ternary device has an increased LDR of 145 dB with a deviation point of 3×10^{-9} W cm^{-2}. It is noted that the LDR value of 145 dB is in the forefront of the reported values so far in all polymer photodiodes.[23,25,27,30–32]

Furthermore, the response speed of the binary and ternary devices is evaluated in terms of -3 dB frequency. -3 dB frequency defines the bandwidth at which the magnitude of the signal is attenuated to -3 dB from the maximum amplitude. As shown in Figure 2f, the binary device based on the newly designed acceptor has exhibited at -3 dB frequency of ≈87 kHz and has been increased to 100 and 130 kHz while gradually increasing the PY-IT content (1:1:0.2 and 1:0.8:0.4 devices). However, there is a sharp increase in -3 dB frequency value to over 200 kHz when the PY-IT content is further increased in the ternary matrix (1:0.6:0.6). The value for PY-IT based binary device is ≈130 kHz, which is in close comparison with 1:0.8:0.4 ternary device and inferior to 1:0.6:0.6 ternary device. Overall, according to the performance metrics assessments, ternary devices, particularly those with a 1:0.6:0.6 composition, offer a considerable advantage in terms of sensitivity-related metrics and response speed, which places them among the best reported in the literature (Figure S11 and Table S1, Supporting Information).

Having identified that ternary systems exhibit superior performance compared to binary devices, it is crucial to elucidate the mechanism driving this improvement. We have carried out systematic investigation into the possible factors resulting in better performance using ultrafast and sensitive spectroscopies and in-depth morphological characterizations. First, we discuss why the addition of third component to the parental binary systems are resulting in lower J_d. Trap density has been identified as a noticeable contributor in controlling the current at lower light intensities or under dark conditions and several other publications addressed the detrimental impacts of traps in charge transport,[33] charge recombination,[34] and overall charge dynamics.[35] Charge traps can originate from various sources, including morphological and structural defects, chemical impurities introduced during material synthesis, environmental contamination, and light-induced material degradation.[36] It is noted that the term "traps" used here indicates "deep traps" which are significantly further away from HOMO and LUMO levels and the carriers captured in these levels are not easily excited back to the transport states.[37] These states frequently serve as the sites for the recombination centers, resulting in reduced carrier lifetime, limited carrier and exciton diffusion length and so on.[37] Thus, reduction of deep trap-density in photodiodes has a pivotal role in improving the figures of merit.[36,38] In a detailed investigation, Kublitski et al. reported the interplay between charge transfer (CT) state and trap state as a source of dark current at voltages relevant for OPDs.[39] Considering the possible influence of traps, we have probed the trap state distribution on an actual working device using sensitive-EQE (s-EQE) spectroscopy. Localized trap state densities are typically four to six orders of magnitude lower than states above the transport energy, and our s-EQE system is capable of detecting photocurrent (down to the picoampere range) from the photoexcited trap states. In the normalized EQE spectra given in Figure 2g, the sub-bandgap region (<1.4 eV) can be mainly divided as two different plateaus, belonging to the band tail and CT states (1.4 eV > CT > 1.06 eV), and deep intra-gap trap state (<1.05 eV). A noticeable separation between CT state and trap state is shown in the 1:1.2:0 binary system, and both states are separated by a region with a flat plateau, and interestingly a similar trend is also seen in the 1:0:1.2 binary system. However, such a clear distinction between CT and trap

states are not present in ternary system, or the magnitude of trap state distribution is relatively lower in ternary systems, serving as a strong reason for the suppressed dark current in ternary systems. The findings obtained from s-EQE have been substantiated through additional verification using admittance spectroscopy. This technique involves determining the energetic distribution of trap density (N_t) by analyzing the capacitive response of these states (Figure S12a, Supporting Information), whose occupation varies with signal modulation.[39–41] In accordance with the s-EQE observation, the ternary devices have lower trap density than the 1:1.2:0 binary control device, confirming the influence of traps in reducing the dark current (Figure 2h). Observations from s-EQE and admittance spectroscopy are further supported by the trap-density calculation from space charge limited current (SCLC) analysis of electron only devices as shown in Figure S12b (Supporting Information). In addition to trap density, the shunt resistance (R_{sh}) can also affect the magnitude of dark current.[11] Analysis of the area-normalized differential resistance-voltage plot reveals the shunt resistance (R_{sh}) in the vicinity of 0 V (Figure S12c, Supporting Information). Notably, R_{sh} tends to be higher for ternary devices than their binary counterparts, resulting in a reduction of leakage pathways. Thus, the incorporation of a high bandgap material into the parental binary narrow bandgap system leads to a decreased trap density and fewer leakage pathways, consequently resulting in lower dark current.

Next, we used fs-transient absorption spectroscopy (TAS) to investigate the underlying charge carrier dynamics in the binary and ternary blends on an ultrafast time scale as well as the kinetic restrictions of device performance.[42,43] The pseudo 2D contour maps and spectral line cuts where shown in Figures S13 and S14 (Supporting Information) while the corresponding kinetics extracted where plotted in Figure 2i. The selected probe range for singlet excitons upon 800 nm excitation wavelength is referenced to the absorption profile of acceptor molecules while the CT and polarons transport are probed on the range corresponding to PBDB-T polarons. Based on most of the blend composition ratios, it appears that the addition of PY-IT does not significantly influence the CT and singlet excitons dissociation dynamics that is probably due to just slightly faster kinetics for PY-IT binary when compared to PZF-V binary. Interestingly, for 1:0.6:0.6 composition ratio, the excitons dissociation is evidently much faster than the binary counterparts and other ternary blend ratios. This is in parallel to the discussed device metrics wherein faster response time and enhanced photocurrent generation is observed in 1:0.6:0.6 ternary device than the binary system. A similar trend can be observed on the basis of polarons generation, which is subsequent to excitons dissociation. Meanwhile, upon monitoring the polarons decay dynamics, PY-IT binary exhibits a much slower recombination than PZF-V binary. Likewise, ternary blends also benefit with such suppressed recombination characteristics, consistent to the observed reduction in traps density. Overall, on the basis of charge carrier dynamics, it is suggestive that properly tuning the ternary composition ratio (i.e., 1:0.6:0.6) in PBDB-T:PZF-V:PY-IT system will enable to take advantage of faster excitons dissociation and reduced polarons recombination to demonstrate a champion device performance.

To explore the morphology evolution endowed by ternary strategy from the point of thin-film crystallization features, neat films and blend films are all studied by grazing incidence wide-angle X-

ray spectroscopy (GIWAXS) experiments.[44–46] The 2D patterns of neat films and related line-cuts along in-plane (IP) and out-of-plane (OOP) directions are given in Figure S15 (Supporting Information). The peak analysis is enabled by applying gaussian function fitting for each region, specifically lamellar and $\pi–\pi$ region. The fitting curves are demonstrated from Figures S16–S18 (Supporting Information) for PBDB-T, PZF-V and PY-IT, respectively. All three materials have face-on orientation generally, indicative of similar molecular packing motifs and good structural compatibility.[47] PBDB-T exhibits the strongest IP direction lamellar diffraction signal thus it dominates the long-range packing in blend films. It also contains two separate peaks contributing together along this direction, corresponding to d-spacings of 22.9 and 21.4 Å, with coherence length (CL) values of 135.1 and 105.9 Å. In comparison, PZF-V and PY-IT exhibit (100) characteristic peaks here at 0.359 Å^{-1} (17.5 Å d-spacing), and 0.306 & 0.385 Å^{-1} (20.5 Å & 16.3 Å), respectively. Meanwhile, their own CLs are only 27.8, 71.6, and 49.2 Å. Polymer acceptors have poorer ordering in long distance packing, which further assures PBDB-T's dominance there. For OOP direction, PBDB-T's main $\pi–\pi$ stacking peak is found at ≈1.63 Å^{-1}, and a more tighter packing signal (very small intensity) at ≈1.75 Å^{-1}. In contrast, PZF-V and PY-IT both exhibit a wide peak with larger width (≈1.48 Å^{-1}, 0.759 Å^{-1}; ≈1.52 Å^{-1}, 0.779 Å^{-1}), and a narrower yet less intense peak (≈1.58 Å^{-1}, 0.284 Å^{-1}; 1.59 Å^{-1}, 0.276 Å^{-1}). Therefore, blend film's OOP directional $\pi–\pi$ stacking signals are supposed to be co-contributed by donor and acceptors at 1.5-1.7 Å^{-1} region. Subsequently, the results of blend films are demonstrated in **Figure 3**, where the 2D patterns, component dependent crystalline parameter variations, and (100) peak's polar angle intensity distribution. The peak analyses are elaborated in Figure S19 (Supporting Information). The OOP lamellar peak is merged by PBDB-T's and PZF-V's and only PBDB-T:PY-IT binary film exhibits two separated lamellar peaks, possibly due to insufficient miscibility and PY-IT's smaller d-spacing value. As for $\pi–\pi$ stacking peak of this direction, the background peak and main peak of each film display no significant d-spacing value change, while PY-IT's ratio increase leads to CL value promotion but a drop in g parameter.[48] Then, it can be claimed that adding PY-IT into PBDB-T:PZF-V system cannot change the initial crystallization characteristics until its component comes up to 50% in acceptors, and its intrinsically higher CL is helpful to more efficient charge transport, which is proven by ternary device's superior performance. The IP directional parameter change is more complicated. However, the general tendency can be summarized as PY-IT is negative to the ordering of $\pi–\pi$ stacking yet improve that of the lamellar packing. Therefore, PBDB-T:PZF-V is intrinsically advantageous in IP directional charge transport while PY-IT based binary system is good at OOP transport. The ternary blend can simultaneously have favorable crystalline features on both directions. This is further supported by polar angle analysis, where ternary film's face-on/edge-on ratio is in between two binary counterparts.

Then, we paid attention to 10 nm scale morphology characteristics by utilizing atomic force microscopy (AFM) and grazing incidence small-angle X-ray scattering (GISAXS) measurements.[49–51] The images are given in **Figure 4**, Figures S20 and S21 (Supporting Information) respectively. PZF-V tends to form strong nano-fibers with PBDB-T in film. In contrast,
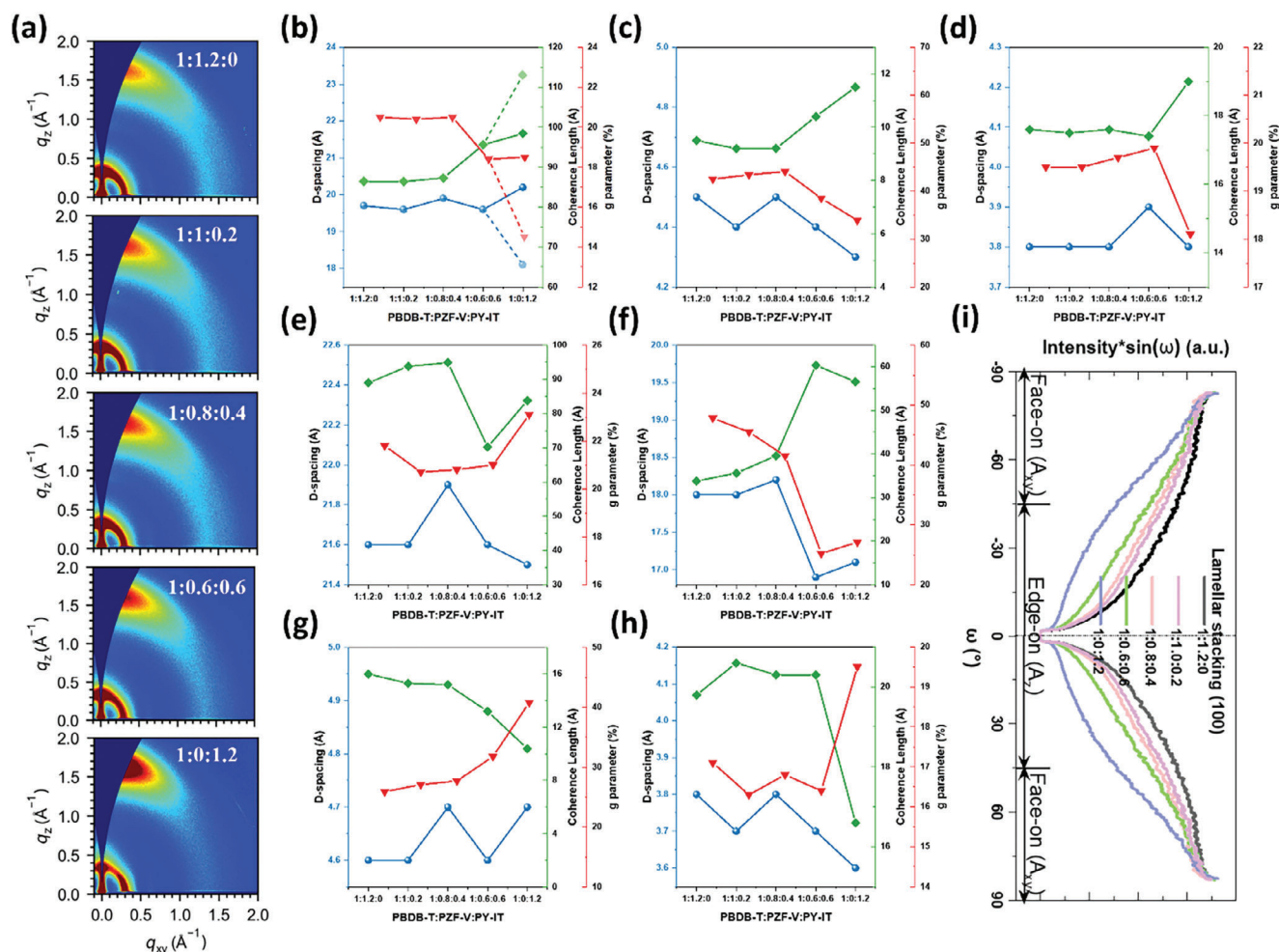
Figure 3. a) 2D GIWAXS patterns of blend films based on all ratios studied here. The crystalline parameter variation of all ratio blend films for b) OOP directional lamellar peaks, c) OOP directional π−π stacking peak [1], d) OOP directional π−π stacking peak [2], e) IP directional lamellar peak [1], f) IP directional lamellar peak [2], g) IP directional π−π stacking peak [1], and h) IP directional π−π stacking peak [2]. i) The orientation analysis upon lamellar diffraction ring of all systems.

PY-IT can bring more sophisticated network structure. The phase separation is then quantitatively studied by Debye-Anderson-Brumberger (DAB) model fitting. The results declared there exists no significant change for IP directional phase separation with or without PY-IT. Thereby, the strong fiber formed by PZF-V binary film is impure phase instead, which means PZF-V is highly miscible with PBDB-T, and serves as "guest" in PBDB-T's own polymer matrix. By adding some PY-IT, the true donor-acceptor phase separation shows up, with tight intertwined, which is supposed to be an ideal structure for effective charge transport and recombination minimization. The miscibility issue is further confirmed by contact angle measurement (Figure S22, Supporting Information) and related surface tension calculation. According to two algorithms (OWRK and Wu), PBDB-T and PZF-V have very close surface tensions, while that of PY-IT is significantly smaller. Thermodynamically, PZF-V is thereby well miscible with PBDB-T, and PY-IT tends to separate more from donor polymer's phase. This is also consistent with GIWAXS's results. We also examined the aspects that may contribute to ternary devices having a faster response time than binary devices. Trap density is known

to have a critical influence on response speed, especially at lower light intensity, and is already demonstrated to be lower for ternary devices. It has also been reported by Saggar and coworkers that the limiting factor for the temporal response speed is the photogenerated slower charge carrier from the device.[52] Thus, the electron and hole mobilities of the pristine and different blend compositions are estimated using SCLC method and the results are given in Figure S23 (Supporting Information). The hole mobility of pristine PBDB-T is 5.5×10^{-3} cm^{2}V^{-1}s^{-1}, the electron mobility of the PY-IT is 3.8×10^{-3} cm^{2}V^{-1}s^{-1} and that of PZF-V is 3.0×10^{-3} cm^{2}V^{-1}s^{-1}. When it comes to the hole mobility of the different compositions, the hole mobility is highest for 1:1.2:0 binary blend and is least for 1:0:1.2 composition and the ternary blends have a value in between these two binary blends. Regarding electron mobility, the trend is just reversed, but the ternary devices maintain a value in between the binary blends. It is worth noting from Figure S23c,f (Supporting Information) that the 1:0.6:0.6 blend has better electron-hole mobility balance and it may be contributing to efficient charge transport and thus fastest response speed among the different compositions studied

**ADVANCED
SCIENCE NEWS**

www.advancedsciencenews.com

**ADVANCED
MATERIALS**

www.advmat.de
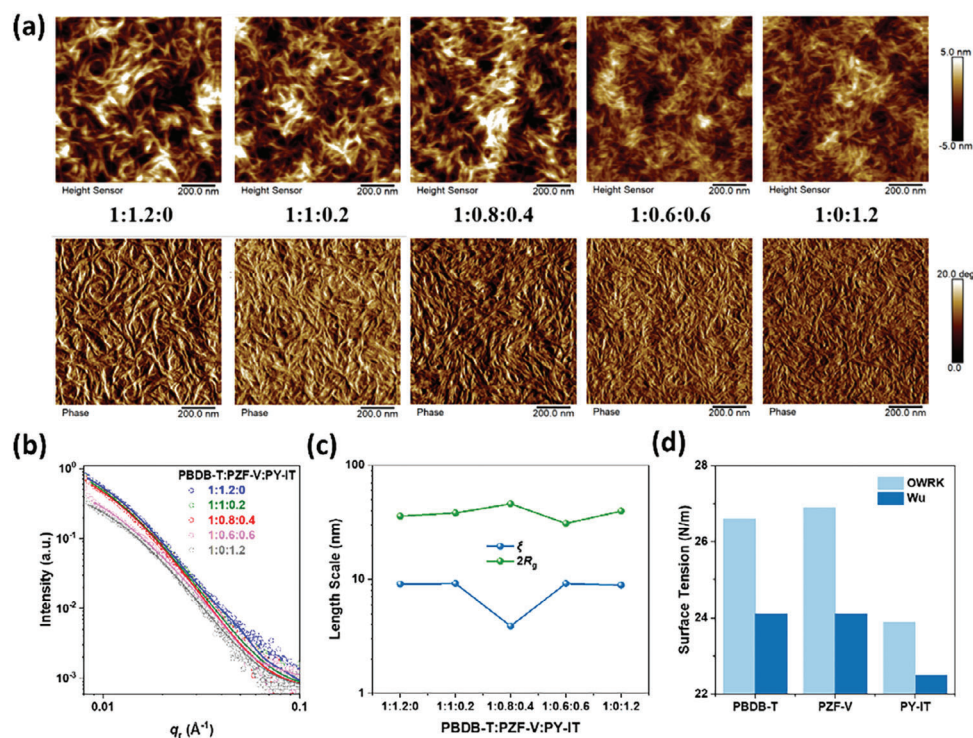
Figure 4. a) AFM height and phase images of active layers. b) IP GISAXS intensity profiles and fitting lines. c) Calculated phase separation parameters. d) Contact angle experiment derived surface tension values of PBDB-T, PZF-V and PY-IT.

in this work.[52] In short, the PY-IT addition to the binary matrix of PBDB-T:PZF-V system positively influences the photodetector in the following ways: 1) reduces the trap density and thereby minimizing the dark and noise currents and improving the detection characteristics in the low light conditions, 2) improving the crystalline features and enhancing the donor-acceptor phase separation and 3) appropriate PY-IT content addition establishes an electron-hole mobility balance. All these factors combinedly result in reduced charge recombination and enhanced transport characteristics, resulting in overall better photodetection metrics for ternary devices.

Although many of the performance metrics are significantly improved over the period, operational stability, specifically illumination and heat stabilities remain a major concern for OPDs.[53] Change in dark current with illumination/heat stress history is considered as a major hurdle to achieve consistent figures of merit.[54] Thus, we explored the illumination and heat stabilities of binary devices and representative ternary device (1:0.6:0.6) for about two hours and the J_d was measured in 30 min intervals. From figure S24a,b (Supporting Information), all three devices have identical trends in terms of illumination stability and heat stability. The change in J_d happens in the first 30 min and there after remains almost constant. The addition of a third component does not have any significant influence in terms of improving the operational stability but overall exhibit appreciable stability. Moreover, a comparison between NFSMA based PD and a representative all polymer PD is carried out in terms of operational stability. NFSMA based device (PBDB-T:BO-4Cl) and its operational stability (illumination and heat stress) is compared with 1:0.6:0.6 ternary all polymer PD. In both systems, the donor material and

the entire device architecture remains same, and the only difference is in terms of the acceptor materials used, providing a reliable comparison of values. When considering the stability under illumination, both types of devices have an initial increase in J_d values in the first 30 min and the change in J_d with the illumination saturates after that up to two hours of illumination (Figure S24c, Supporting Information). When evaluating heat stability, the all-polymer PD devices demonstrate superior stability compared to the NFSMA-based PDs (Figure S24d, Supporting Information). Specifically, the all-polymer PD systems show a negligible change in J_d values from 30 min to two hours under thermal stress. In contrast, the NFSMA system undergoes a more pronounced change, with J_d increasing by approximately two orders of magnitude after heat stress. In conclusion, while both systems exhibit comparable stability under illumination, the all-polymer PD systems have a clear advantage in terms of heat stability over the NFSMA system.

Moving forward, we have developed a smart PPG sensor with enhanced capabilities using our optimized all-polymer ternary device, showcasing a practical prototype for real-world implementation. PPG sensor is a low-cost non-invasive device designed to measure fluctuations in blood volume within the microvascular tissue.[55] It is commonly employed for monitoring physiological parameters such as heart rate and oxygen saturation.[56] In this work, we present a cuffless blood pressure (BP) estimation method for continuous non-invasive BP monitoring which includes data collection using OPD sensor, data filtering and a machine learning model development (**Figure 5a**). Figure S25 (Supporting Information) depicts the setup schematic, which includes an NIR LED light source

**ADVANCED
SCIENCE NEWS**

www.advancedsciencenews.com

**ADVANCED
MATERIALS**

www.advmat.de
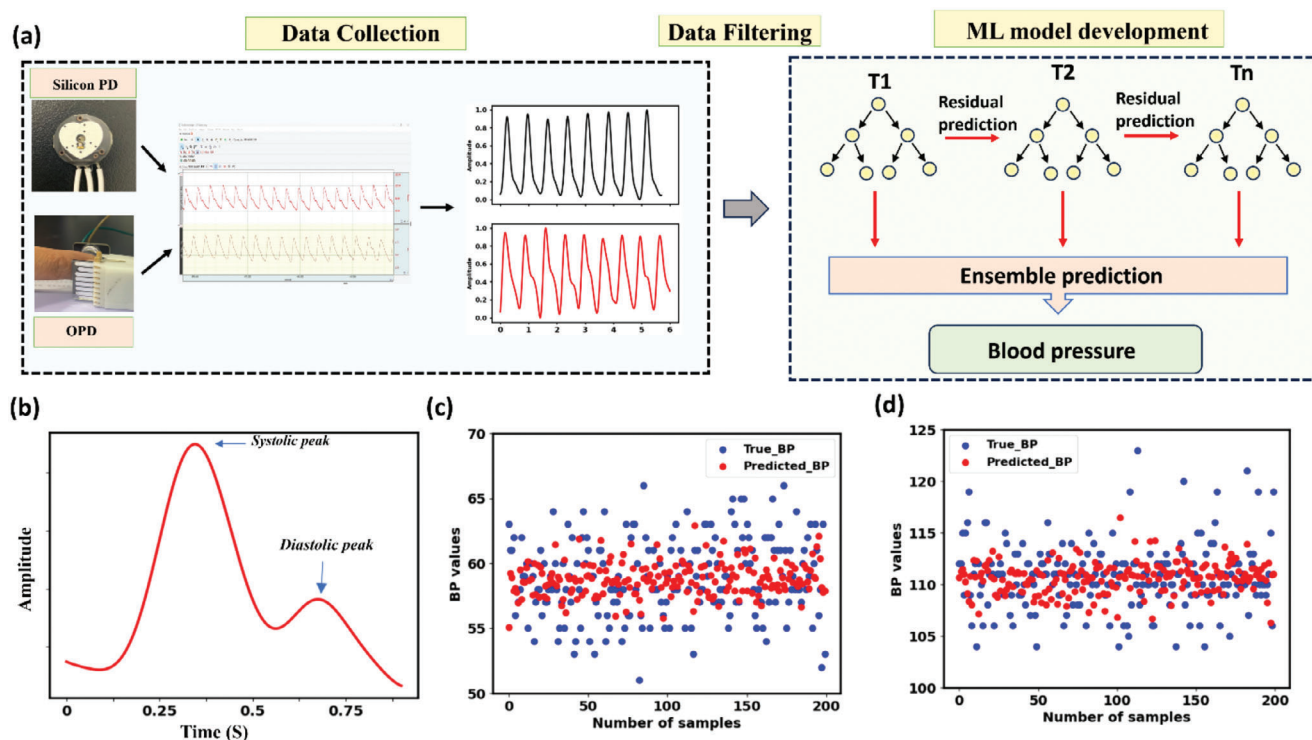
Figure 5. a) Process flow of BP estimation which includes data collection using corresponding photodiodes, data filtering and machine learning model development. b) Systolic and diastolic peaks in a typical PPG signal. True BP ranges in the test dataset and corresponding predicted c) systolic BP and d) diastolic BP.

(830 nm), photodetector (silicon or organic), and a BioPAC (BioPAC System, Inc. MP160) as hardware components for data collection. For the demonstration purpose, we have collected the PPG signal of healthy volunteers using an organic PD functioning at self-power mode and a commercial silicon diode working at a biased mode for comparison. The signal acquired has a sampling rate of 2000 Hz, and signals recorded with both diodes exhibit the characteristic systolic and diastolic peaks as illustrated in Figure 5b. It is interesting to note that the OPD can be placed at a distance up to 10 cm from the patient, allowing for unobtrusive continuous vital signal monitoring, which is not achievable with standard silicon diode of the same setup. 17 volunteers were selected to study the BP variations during the continuous BP measurement. Commercial equipment (BioPAC) equipped with CNAP monitor, which has been proved providing clinically acceptable accuracy, attached on the same volunteers to measure reference BP. Moreover, measured systolic blood pressure (SBP) and diastolic blood pressure (DBP) range was 99–123 mmHg and 49–68 mmHg, respectively (Figure 5c,d).

In medical data preprocessing, like with PPG signals, the focus is on refining, improving, and distilling insights from raw data. Filtering plays a pivotal role in eradicating unwanted interference, heightening signal clarity, and spotlighting relevant details. For PPG signals, a butterworth bandpass filter is used, often set at a high-pass cutoff frequency of 5 Hz and a low-pass cutoff of 0.5 Hz. These specific settings retain vital frequency components while diminishing extraneous noise. Addressing baseline wander, a frequent issue in physiological signals, involves targeted techniques to eliminate low-frequency fluctuations that

could mask the underlying waveform. Clearing baseline wander aids in better interpreting the data. Harmonizing temporal alignment across signals from various sources or patients is crucial for precise comparative analysis. Normalization steps, standardizing signal amplitude and scale, are pivotal, especially when getting data from diverse subjects or timeframes. Normalization guarantees a consistent ground for analysis, enabling more insightful comparisons.

Acknowledging the potential pitfalls of overfitting in expansive models like deep neural networks, we sought a simpler approach for potentially improved performance. In this pursuit, ensemble learning emerged as a viable solution to mitigate the risks associated with overfitting. Specifically, we turned to the Gradient Boosting Trees algorithm, which amalgamates predictions from several simpler models to craft a robust and effective final model.[57,58] This approach not only surpasses the performance of individual learners but also demands less computational time compared to the intricacies of a deep neural network.[57] Consequently, it was our chosen cornerstone for BP estimation. In our endeavor, each piece of collected data underwent meticulous preprocessing, with a strategic division into training and test sets at a ratio of 4:1. The subsequent testing phase unveiled promising results, with a mean absolute error of 2.9 ± 2.5 mmHg for SBP and 2.4 ± 2.2 mmHg for DBP. These figures comfortably align within the standards set by the AAMI (Error: $\leq \pm 5$ mmHg, Std: $\leq \pm 8$ mmHg), affirming the precision of our model.[59] Further reinforcing our findings, the Bland-Altman plot demonstrated that our data confidently resides within the 95% confidence limits, providing assurance regarding the consistency between

**ADVANCED
SCIENCE NEWS**

www.advancedsciencenews.com

**ADVANCED
MATERIALS**

www.advmat.de

actual measurements and our estimated BP values (Figure S26, Supporting Information)

Beyond healthcare, we demonstrate another advanced functionality of the proposed all polymer PD in computational imaging. Contemporary detector technologies have found their perfect testing ground in computational imaging or SPI, which has facilitated the creation of affordable imaging systems operating at various electromagnetic spectrum wavelengths. As the name suggests, SPI uses a single-pixel detector in contrast to the array of millions of detector pixels used in modern cameras.[60] This is made feasible by a sequence of mask patterns that are used to filter the scene and the associated transmitted intensity measurements that are captured by the single-pixel detector. Consequently, hardware improvements and computational methods play an equal role in the success of SPI, and the capability of the all-polymer PD is quantitively compared with the default silicon detector of the setup. However, excluding a few preliminary studies that tested the capability of OPDs in SPI, most of the studies on SPI used commercial silicon diodes and improved the computational side of the SPI. Here, we have tested the performance of all-polymer PD in a variety of imaging scenarios, ranging from the initial test in free space to the complex imaging environments, like when the imaging target is in the detector's non-line of sight (NLOS) and when light has to travel through scattering media.

The compatibility check of the all-polymer PD in high-spatial resolution SPI is done at free space, wherein the path between the target and the detector is free of any obstructions as given in the schematic diagram in Figure S27 (Supporting Information). **Figure 6**a depicts the image reconstruction process while Figure 6b,c show the resulting patterns (128 × 128 pixels) and Fourier spectra. The USAF 1951 resolution target is reconstructed in free space using the default silicon PD and the all-polymer PD and is given in Figure 6d. It is to be noted that, at 10% sampling ratio, both the detectors can reconstruct the shape, and a clearer and sharper image is reconstructed at 50% and 100% sampling ratios. The reconstruction capability of large area all-polymer PD is in close comparison with that of commercial silicon diodes. Next, the OPD performance is tested at a more complex imaging environment wherein dual ground glass diffusers (scattering grits) are placed in between the target and the detector such that the light transmitted through the target must pass through scattering media before being detected by the detector (Figure S28, Supporting Information). The advantage of SPI can be seen in this scenario wherein the traditional camera (CCD or CMOS) cannot work properly, but the OPD can reconstruct the image with ease using SPI (Figure 6e). In this complex scenario, both commercial and the proof-of-concept all-polymer PD devices work equally well.

Next, the detection capability of all-polymer PD is tested in NLOS, which aims to rebuild the target that is out of the observer's direct line of sight. NLOS imaging has a potential to be used in robotic vision, autonomous vehicles, medical imaging, remote sensing, and rescue operations, among other areas.[61] Figure 6g shows a schematic representation of the NLOS measurement setup, where the light transmitted from the target is blocked by a wall and then the reflected light from the wall is collected by the detector. In other words, the target and detector are at NLOS, being blocked by the wall. Figure 6f shows the re-

constructed image when PDA100A2 and all-polymer PD are respectively used, and both of them are capable of quality image reconstruction at this complex scenario.

Having found that the all-polymer PD is comparable in performance with the commercial silicon diode, it is important to compare the performance quantitatively. We have derived contrast-to-noise ratio of both detectors at different imaging scenarios defined by,

$$CNR = \frac{\left|\mu_f - \mu_b\right|}{\sqrt{\sigma_f{}^2 + \sigma_b{}^2}} \qquad (4)$$

where μ_f and μ_b denote respectively average intensity of feature part and background part in the reconstructed images, and σ_f and σ_b denote respectively standard deviation of feature part and background part in the reconstructed images. In Figure 6h–j, for all three imaging scenarios, the all-polymer PD exhibits a competitive CNR that is within 5% difference with that of commercial silicon diodes. The difference is even less for both scattering and NLOS scenarios, primarily because the proof-of-concept device's active sensing area is larger than silicon diode's and can detect captured/reflected light more effectively. The performance can be deemed excellent, given that the all-polymer PD operates in self-power mode and could potentially be significantly less expensive than commercial silicon diodes.

3. Conclusion

An all-polymer infrared organic photodiode with outstanding performance metrics is demonstrated by efficiently tuning the morphology and exciton behaviors. The performance of the binary PD consisting of a newly designed polymer acceptor is further boosted by adding a second acceptor material with a relatively larger bandgap. The third component is advantageous in forming the ternary system with reduced trap density, manipulating charge transport in both IP and OOP directions, stimulating efficient donor-acceptor phase separation and balancing electron-hole mobility. These improved photophysical characteristics have resulted in figures of merit that are among the best recorded values in OPDs, particularly in the all-polymer PD subcategory. The detection metrics maintained a balance between sensitivity and speed, such as ultra-low noise current of 6 fA Hz$^{-1/2}$, experimentally determined specific detectivity approaching 10^{13} Jones, LDR of 145 dB and a fast temporal response speed of 220 kHz. The optimized device has been used to realize advanced real-world applications, such as a non-invasive BP monitoring system employing the PPG sensor and a custom-designed machine learning model. Furthermore, the competitive performance of all-polymer NIR photodetectors, rivaling that of commercial silicon diodes, is further indicated by the demonstration of a high spatial resolution computational camera prototype in a variety of complex imaging settings, including scenarios where the object is obscured by a wall or within a scattering medium.

4. Experimental Section

Device Fabrication and Characterizations: Photodiodes were fabricated in a traditional structure of ITO/PEDOT:PSS/active layers/PFN-Br/Ag.

**ADVANCED
SCIENCE NEWS**

www.advancedsciencenews.com

**ADVANCED
MATERIALS**

www.advmat.de
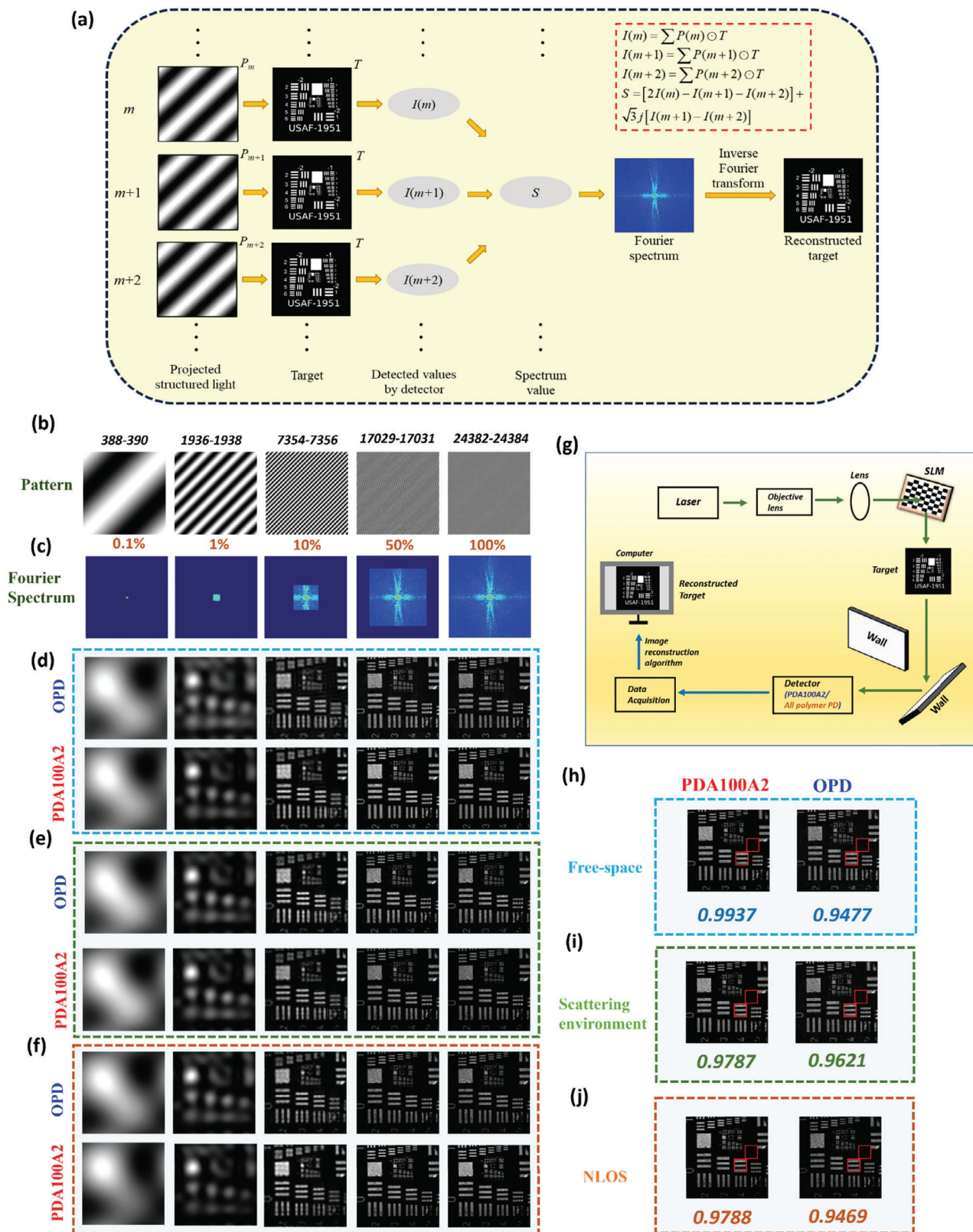
Figure 6. a) A detailed flow chart of the image reconstruction process. b) The generated patterns and c) Fourier spectra at different sampling ratios. The reconstructed images at different sampling ratios using all-polymer PD and PDA100A2 at d) free-space e) scattering environment and f) NLOS. g) Schematic representation of the single pixel imaging setup in the NLOS. The quantitative comparison of all-polymer PD and PDA100A2 via CNR at h) free-space i) scattering medium and j) NLOS.

The ITO substrates were first scrubbed by detergent and then sonicated with deionized water, acetone and isopropanol subsequently, and dried overnight in an oven. The glass substrates were treated by UV-Ozone for 30 min before use. PEDOT:PSS (Al4083 from Hareus) was spin-cast onto the ITO substrates at 6000 rpm for 30 s, and then dried at 170 °C for 15 min. The PBDB-T:PZF-V:PY-IT blends (weight ratios are: 1:x:1.2-x) were dissolved in chloroform (the concentration of donor was 15 mg mL^{-1}), with 1-chloronaphthalene (2 vol%) as additive, and stirred for 1 h. The blend solution was spin-cast at 1500 rpm for 30 s onto PEDOT:PSS film followed by a temperature annealing of 100 °C for 2 min. A thin PFN-Br layer (0.5 mg mL^{-1} in methanol, 2000 rpm) was coated on the active layer, followed by the deposition of Ag (evaporated under 3×10^{-4} Pa through a shadow mask). The optimal active layer thickness measured by a Bruker Dektak XT stylus profilometer was ≈300 nm.

A Keithley 2400 source meter was used to measure the current density-voltage (J-V) in the dark. Utilizing the Enlitech Co., Ltd. spectral response measurement instrument (QE-R), biased EQE and responsivity were measured at 210 Hz chopper frequency. Using a custom-built setup that included a network analyzer (Stanford Research Systems SR770) and a low-noise current preamplifier (Standard Research SR570), noise current was measured in the dark. The corresponding noise current value at 210 Hz was utilized in further calculations to match the equiv. noise bandwidth of the measurements of responsivity. The DSA-100 (KRUSS Germany) contact angle meter was used to measure the films' contact angles. UV–vis absorption spectra were measured using a Shimadzu UV-2500 recording spectrophotometer. AFM measurements were obtained by using a Dimension Icon AFM (Bruker) in a tapping mode. The grazing incidence small/wide angle X-ray scattering (GISAXS/GIWAXS) measurements were carried out with a Ganesha SAXSLAB laboratory instrument using a CuKα X-ray source (8.05 keV, 1.54 Å) and a Pilatus 300K detector. The samples for GIWAXS/GISAXS measurements were fabricated on silicon substrates using the same recipe as for the devices. The incident angle was 0.4° for GISAXS and 0.2° for GIWAXS measurements, respectively. The sample to detector distance (SDD) was set to 1045 and 95 mm for GISAXS and GIWAXS measurement. For the GISAXS images, the DPDAK software was applied to extract the polymer scattering signals. The transformation to q-space, radial cuts for the IP and OOP analysis and azimuthal cuts for the orientation analysis were processed by the MATLAB-based package GIXSGUI.

The frequency response of the device was assessed by illuminating square wave-modulated 830 nm LED light on the all-polymer PD at different frequencies. A low-noise pre-amplifier was used to boost the signal from the OPD, and the amplified transient was then recorded using an oscilloscope (Tektronics MDO 3024) set to 50 Ω load resistance.

An 830 nm monochromatic light source with variable input irradiance was used to illuminate the PD device in order to measure the LDR. By arranging a series of neutral density filters (Thorlabs), the input irradiance was changed. The input power was measured using a calibrated silicon detector (Thorlabs DET100), and the photo response (at −0.1 V) was measured with a lock-in amplifier (Standard Research SR830). Data was acquired using a custom-written LabVIEW program.

The electron and hole mobility were measured by using the method of space-charge limited current (SCLC) for electron-only devices with the structure of ITO/ZnO/active layer/PFN-Br-MA/Ag and hole-only devices with the structure of ITO/PEDOT:PSS-TA/active layers/MoO$_x$/Ag. The charge carrier mobility was determined by fitting the dark current to the model of a single carrier SCLC according to the equation: $J = 9\epsilon_0\epsilon_r\mu V^2/8d^3$, where J is the current density, d is the film thickness of the active layer, μ is the charge carrier mobility, ϵ_r is the relative dielectric constant of the transport medium, and ϵ_0 is the permittivity of free space. $V = V_{app} - V_{bi}$, where V_{app} is the applied voltage, V_{bi} is the offset voltage. The charge carrier mobility was calculated from the slope of the $J^{1/2} \approx V$ curves. The thickness of target layer is well controlled identical to that of PV's active layer.

Transient absorption spectroscopy (TAS) was measured with an amplified Ti:sapphire femtosecond laser (800 nm wavelength, 50 fs, 1 kHz repetition; Coherent Libra) and a Helios pump/probe setup (Ultrafast Systems). The 400 nm pump pulses with a pump fluence of 0.5 or < 3 μJ/cm^2 were obtained by frequency doubling the 800 nm fundamental regenera-tive amplifier output. The white-light continuum probe pulses were generated by focusing a small portion of the regenerative amplifier's fundamental 800 nm laser pulses into a 2 mm sapphire crystal.

Informed written consent was obtained from all participants prior to the commencement of the research in non-invasive BP monitoring.

Reconstruction Algorithm: To reconstruct the object via acquiring its Fourier spectrum, a series of 2D sinusoid patterns was generated with specific spatial frequency (f_x, f_y) and initial phase φ, which can be described by

$$P_\phi(x, y; f_x, f_y) = a + b \cdot \cos(2\pi f_x X + 2\pi f_y Y + \phi) \tag{5}$$

where (x, y) represents the spatial coordinates, a denotes the background intensity and b denotes amplitude modulation.[62]

A photodetector without spatial resolution collects total intensity behind the object, when such structured 2D patterns are projected onto the object, which can be represented by

$$I_\phi(f_x, f_y) = \sum_x \sum_y P_\phi(x, y; f_x, f_y) \odot T(x, y) \tag{6}$$

where $T(x, y)$ denotes an object to be reconstructed and $\odot$ represents an element-wise product. To obtain complex Fourier coefficients, the three-step phase-shifting approach is utilized by sequentially projecting three sinusoidal patterns with the same spatial frequency (f_x, f_y) and different initial phase ($0, \frac{2}{3}\pi, \frac{4}{3}\pi$) described by

$$S(f_x, f_y) = [2I_0(f_x, f_y) - I_{2\pi/3}(f_x, f_y) - I_{4\pi/3}(f_x, f_y)] \\ + \sqrt{3}j[I_{2\pi/3}(f_x, f_y) - I_{4\pi/3}(f_x, f_y)] \tag{7}$$

where j denotes the imaginary unit. After all the complex Fourier coefficients are obtained, inverse Fourier transform (IFT) can be applied to reconstruct the object:

$$\hat{T}(x, y) = \text{IFT}\{S(f_x, f_y)\} \tag{8}$$

where $\hat{T}(x, y)$ denotes a recovered object.

Supporting Information

Supporting Information is available from the Wiley Online Library or from the author.

Acknowledgements

Conflict of Interest

The authors declare no conflict of interest.

Data Availability Statement

The data that support the findings of this study are available from the corresponding author upon reasonable request.

**ADVANCED
SCIENCE NEWS**

www.advancedsciencenews.com

**ADVANCED
MATERIALS**

www.advmat.de

[1] L. Mei, R. Huang, C. Shen, J. Hu, P. Wang, Z. Xu, Z. Huang, L. Zhu, *Adv. Opt. Mater.* **2022**, *10*, 2102656.

[2] A. Rogalski, *Opto-Electron. Rev.* **2012**, *20*, 279.

[3] S. Gielen, C. Kaiser, F. Verstraeten, J. Kublitski, J. Benduhn, D. Spoltore, P. Verstappen, W. Maes, P. Meredith, A. Armin, *Adv. Mater.* **2020**, *32*, 2003818.

[4] S. Park, K. Fukuda, M. Wang, C. Lee, T. Yokota, H. Jin, H. Jinno, H. Kimura, P. Zalar, N. Matsuhisa, *Adv. Mater.* **2018**, *30*, 1802359.

[5] X. Xu, Y. Zhao, Y. Liu, *Small* **2023**, *19*, 2206309.

[6] Y. Zhang, Y. Lang, G. Li, *EcoMat* **2023**, *5*, e12281.

[7] V. Pecunia, D. Natali, M. Caironi, *Organic Photodetectors, Photodetectors*, Elsevier, Amsterdam/New York, **2023**, p. 73.

[8] B. Yin, X. Zhou, Y. Li, G. Hu, W. Wei, M. Yang, S. Jeong, W. Deng, B. Wu, Y. Cao, *Adv. Mater.* **2024**, *36*, 2310811.

[9] M. Yang, B. Yin, G. Hu, Y. Cao, S. Lu, Y. Chen, Y. He, X. Yang, B. Huang, J. Li, *Chem.* **2024**, *10*, 1425.

[10] C. Wang, X. Zhang, W. Hu, *Chem. Soc. Rev.* **2020**, *49*, 653.

[11] J. Huang, J. Lee, J. Vollbrecht, V. V. Brus, A. L. Dixon, D. X. Cao, Z. Zhu, Z. Du, H. Wang, K. Cho, *Adv. Mater.* **2020**, *32*, 1906027.

[12] Y. Wei, H. Chen, T. Liu, S. Wang, Y. Jiang, Y. Song, J. Zhang, X. Zhang, G. Lu, F. Huang, *Adv. Funct. Mater.* **2021**, *31*, 2106326.

[13] J. Fu, Q. Yang, P. Huang, S. Chung, K. Cho, Z. Kan, H. Liu, X. Lu, Y. Lang, H. Lai, *Nat. Commun.* **2024**, *15*, 1830.

[14] Y. Zhang, W. Deng, C. E. Petoukhoff, X. Xia, Y. Lang, H. Xia, H. Tang, H. T. Chandran, S. Mahadevan, K. Liu, P. W. K. Fong, Y. Luo, J. Wu, S. W. Tsang, F. Laquai, H. Wu, X. Lu, Y. Yang, G. Li, *Joule* **2024**, *8*, 509.

[15] L. Wang, C. Chen, Y. Fu, C. Guo, D. Li, J. Cheng, W. Sun, Z. Gan, Y. Sun, B. Zhou, *Nat. Energy* **2024**, *9*, 208.

[16] L. Zhu, M. Zhang, J. Xu, C. Li, J. Yan, G. Zhou, W. Zhong, T. Hao, J. Song, X. Xue, *Nat. Mater.* **2022**, *21*, 656.

[17] J. Fu, P. W. Fong, H. Liu, C.-S. Huang, X. Lu, S. Lu, M. Abdelsamie, T. Kodalle, C. M. Sutter-Fella, Y. Yang, *Nat. Commun.* **2023**, *14*, 1760.

[18] H. T. Chandran, H. Tang, T. Liu, S. Mahadevan, K. Liu, Z. Lu, J. Huang, Z. Ren, F. Liao, Y. Chai, *Mater. Horiz.* **2023**, *10*, 918.

[19] T. Wang, M. Chen, R. Sun, J. Min, *Chem.* **2023**, *9*, p1702.

[20] Y. Zhao, T. Liu, B. Wu, S. Zhang, N. Prine, L. Zhang, S. Pang, B. Yin, L. Ye, X. Gu, *Chem. Mater.* **2021**, *33*, 3746.

[21] X. Huang, Z. Zhao, S. Chung, K. Cho, J. Lv, S. Lu, Z. Kan, *J. Mater. Chem. C* **2022**, *10*, 17502.

[22] J. Qi, W. Qiao, X. Zhou, D. Yang, J. Zhang, D. Ma, Z. Y. Wang, *Macromol. Chem. Phys.* **2016**, *217*, 1683.

[23] P. Sen, R. Yang, J. J. Rech, Y. Feng, C. H. Y. Ho, J. Huang, F. So, R. J. Kline, W. You, M. W. Kudenov, *Adv. Opt. Mater.* **2019**, *7*, 1801346.

[24] Y. Fang, A. Armin, P. Meredith, J. Huang, *Nat. Photonics* **2019**, *13*, 1.

[25] X. Wang, S. Gao, J. Han, Z. Liu, W. Qiao, Z. Y. Wang, *ACS Appl. Mater. Interfaces* **2022**, *14*, 26978.

[26] Z. Zhong, L. Bu, P. Zhu, T. Xiao, B. Fan, L. Ying, G. Lu, G. Yu, F. Huang, Y. Cao, *ACS Appl. Mater. Interfaces* **2019**, *11*, 8350.

[27] Y. Xia, L. E. Aguirre, X. Xu, O. Inganäs, *Adv. Electron. Mater.* **2020**, *6*, 1901017.

[28] Z. Du, H. M. Luong, S. Sabury, A. L. Jones, Z. Zhu, P. Panoy, S. Chae, A. Yi, H. J. Kim, S. Xiao, *Adv. Mater.* **2023**, 2310478.

[29] H. T. Chandran, S. Mahadevan, R. Ma, Y. Tang, T. Zhu, F. Zhu, S.-W. Tsang, G. Li, *Appl. Phys. Lett.* **2024**, *124*, 101113.

[30] X. Wang, Z. Y. Wang, S. Gao, J. Han, Y. Xu, Z. Liu, H. Wang, Y. Zhang, W. Qiao, *Chem. Eng. J.* **2023**, *474*, 145529.

[31] Z. Zhong, K. Li, J. Zhang, L. Ying, R. Xie, G. Yu, F. Huang, Y. Cao, *ACS Appl. Mater. Interfaces* **2019**, *11*, 14208.

[32] X. Xu, X. Zhou, K. Zhou, Y. Xia, W. Ma, O. Inganäs, *Adv. Funct. Mater.* **2018**, *28*, 1805570.

[33] H. T. Nicolai, M. Kuik, G. Wetzelaer, B. De Boer, C. Campbell, C. Risko, J. Brédas, P. Blom, *Nat. Mater.* **2012**, *11*, 882.

[34] S. R. Cowan, W. L. Leong, N. Banerji, G. Dennler, A. J. Heeger, *Adv. Funct. Mater.* **2011**, *21*, 3083.

[35] A. Hofacker, D. Neher, *Phys. Rev. B* **2017**, *96*, 245204.

[36] X. Ma, R. A. Janssen, G. H. Gelinck, *Adv. Mater. Technol.* **2023**, *8*, 2300234.

[37] Z. Liu, Y. Lin, *Polym. Test.* **2024**, *132*, 108387.

[38] H. Thachoth Chandran, C. Yan, G. Li, *Adv. Energy Sustainability Res.* **2022**, *3*, 2200002.

[39] J. Kublitski, A. Hofacker, B. K. Boroujeni, J. Benduhn, V. C. Nikolis, C. Kaiser, D. Spoltore, H. Kleemann, A. Fischer, F. Ellinger, *Nat. Commun.* **2021**, *12*, 551.

[40] S. Khelifi, K. Decock, J. Lauwaert, H. Vrielinck, D. Spoltore, F. Piersimoni, J. Manca, A. Belghachi, M. Burgelman, *J. Appl. Phys.* **2011**, *110*.

[41] K. Liu, Q. Liang, M. Qin, D. Shen, H. Yin, Z. Ren, Y. Zhang, H. Zhang, P. W. Fong, Z. Wu, Z. Wu, J. Huang, J. Hao, Z. Zheng, S. K. So, C.-S. Lee, X. Lu, G. Li, *Joule* **2020**, *4*, 2404.

[42] B. Zou, W. Wu, T. A. Dela Peña, R. Ma, Y. Luo, Y. Hai, X. Xie, M. Li, Z. Luo, J. Wu, *Nanomicro. Lett.* **2024**, *16*, 1.

[43] T. Liu, Z. Jia, Y. Song, N. Yu, Q. Lin, C. Li, Y. Jia, H. Chen, S. Wang, Y. Wei, *Adv. Funct. Mater.* **2023**, *33*, 2301167.

[44] J. Rivnay, S. C. Mannsfeld, C. E. Miller, A. Salleo, M. F. Toney, *Chem. Rev.* **2012**, *112*, 5488.

[45] P. Müller-Buschbaum, *Adv. Mater.* **2014**, *26*, 7692.

[46] R. Ma, X. Jiang, J. Fu, T. Zhu, C. Yan, K. Wu, P. Müller-Buschbaum, G. Li, *Energy Environ. Sci.* **2023**, *16*, 2316.

[47] Y. Yang, W. Chen, L. Dou, W.-H. Chang, H.-S. Duan, B. Bob, G. Li, Y. Yang, *Nat. Photonics* **2015**, *9*, 190.

[48] K. Zhou, K. Xian, R. Ma, J. Liu, M. Gao, S. Li, T. Liu, Y. Chen, Y. Geng, L. Ye, *Energy Environ. Sci.* **2023**, *16*, 5052.

[49] D. Li, N. Deng, Y. Fu, C. Guo, B. Zhou, L. Wang, J. Zhou, D. Liu, W. Li, K. Wang, *Adv. Mater.* **2023**, *35*, 2208211.

[50] R. Ma, H. Li, T. A. D. Peña, X. Xie, P. W. K. Fong, Q. Wei, C. Yan, J. Wu, P. Cheng, M. Li, *Adv. Mater.* **2023**, *36*, 2304632.

[51] Y. Xiao, X. Lu, *Mater. Today Nano* **2019**, *5*, 100030.

[52] S. Saggar, S. Sanderson, D. Gedefaw, X. Pan, B. Philippa, M. R. Andersson, S. C. Lo, E. B. Namdas, *Adv. Funct. Mater.* **2021**, *31*, 2010661.

[53] J. Liu, M. Gao, J. Kim, Z. Zhou, D. S. Chung, H. Yin, L. Ye, *Mater. Today* **2021**, *51*, 475.

[54] J. Huang, J. Lee, H. Nakayama, M. Schrock, D. X. Cao, K. Cho, G. C. Bazan, T.-Q. Nguyen, *ACS Nano* **2021**, *15*, 1753.

[55] L. Zhao, C. Liang, Y. Huang, G. Zhou, Y. Xiao, N. Ji, Y.-T. Zhang, N. Zhao, *npj Digit. Med.* **2023**, *6*, 93.

[56] J. V. Dcosta, D. Ochoa, S. Sanaur, *Adv. Sci.* **2023**, *10*, 2302752.

[57] J. Li, H. Jia, J. Zhou, X. Huang, L. Xu, S. Jia, Z. Gao, K. Yao, D. Li, B. Zhang, *Nat. Commun.* **2023**, *14*, 5009.

[58] E. Guldogan, F. H. Yagin, A. Pinar, C. Colak, S. Kadry, J. Kim, *Sci. Rep.* **2023**, *13*, 22189.

[59] H. Tang, G. Ma, L. Qiu, L. Zheng, R. Bao, J. Liu, L. Wang, *Cardiovasc. Eng. Technol.* **2024**, *15*, 39.

[60] M. P. Edgar, G. M. Gibson, M. J. Padgett, *Nat. Photonics* **2019**, *13*, 13.

[61] X. Liu, J. Wang, L. Xiao, Z. Shi, X. Fu, L. Qiu, *Nat. Commun.* **2023**, *14*, 3230.

[62] Z. Zhang, X. Ma, J. Zhong, *Nat. Commun.* **2015**, *6*, 6225.